Research paper

Chemical recovery of spent copper powder in laser powder bed fusion

Alistair Speidel [a,*], Leonidas Gargalis [b], Jianchao Ye [c], Manyalibo J. Matthews [c], Adriaan Spierings [d], Richard Hague [b], Adam T. Clare [a], James W. Murray [a]

[a] Advanced Component Engineering Laboratory (ACEL), Faculty of Engineering, University of Nottingham, Nottingham NG8 1BB, UK
[b] Centre for Additive Manufacturing (CfAM), Faculty of Engineering, University of Nottingham, Nottingham NG8 1BB, UK
[c] Materials Science Division, Physical and Life Sciences Directorate, Lawrence Livermore National Laboratory (LLNL), 7000 East Avenue, Livermore, CA 94550, USA
[d] Inspire AG, Innovation Center for Additive Manufacturing Switzerland (ICAMS), Fürstenlandstrasse 122, 9014 St. Gallen, Switzerland

ARTICLE INFO

ABSTRACT

In laser powder bed fusion (LPBF), recovered unfused powder from the powder bed often degrades upon sequential processing through mechanisms like thermal oxidation and particle satelliting from ejected weld spatters and particle-laser interactions. Given the sensitivity of LPBF performance and build quality to powder properties, spent powder is generally discarded after a few build cycles, especially for materials that are sensitive towards surface oxidation. This increases feedstock material costs, as well as costs associated with machine downtime during powder replacement. Here, a new method to chemically reprocess spent LPBF metal powder is demonstrated under ambient conditions, using a heavily oxidised Cu powder feedstock recovered from prior LPBF processing as a model material. This is compared to an equivalent virgin Cu powder. The near-surface powder chemistry has been analysed, and it is shown that surface oxide layers present on spent Cu powder can be effectively reset after rapid reprocessing (from 5 to 20 min). Diffuse reflectance changes on etching, reducing for gas-atomised virgin Cu powder due to the formation of anisotropic etch facets, and increasing for heavily oxidised spent Cu as the highly absorptive oxide layers are removed. The mechanism of powder degradation for moisture sensitive materials like Cu has been correlated to the degradation of LPBF deposits, which manifests as widespread and extensive porosity. This extensive porosity is largely eliminated after reprocessing the spent Cu powder. Chemically etched spent powder is therefore demonstrated as a practical feedstock in LPBF in which track density produced is comparable to virgin powder.

1. Introduction

Powder-based additive manufacturing (AM) methods such as laser powder bed fusion (LPBF) enable the manufacture of net and near-net shape complex parts. In principle, this approach minimises material usage. However, residual feedstock material on or around the build plate often degrades upon sequential processing, by various mechanisms of spatter [1], thermal oxidation and segregation [2], particle fusion (satelliting) [3], and atmospheric removal of small particles during handling [4]. Particle size distributions affect the flowability and the packing density of the powder bed [5,6], therefore final part density and build quality will also be affected by powder reuse [7]. As such, used powder is often discarded and not recycled after a predetermined number of processing cycles (Fig. 1a) [8].

There is a clear economic case for powder lifetime extension, and this case is stronger for bespoke powders or exotic compositions. In addition,

metal powder manufacturing processes, the most common being water and gas atomisation, consume significant amounts of energy in the context of the whole life cycle [9]. Avoidance of new powder manufacture is therefore important for the economic and environmental case for AM technologies. In addition, the correct end-of-life (EoL) point for a powder can be challenging to identify, given the dependence of powder degradation on multiple complex variables [10]. For these reasons, methods to enable greater powder reuse are increasingly important. Plasma spheroidisation [11] has been applied to reprocess EoL powders used in AM, allowing powder morphologies to return to the initial supply states, improving flowability and packing density. However, processes that involve the melting of the initial powder are energy intensive [9]. Processes involving powder re-melting can generate new powder size distributions and morphologies, producing variations in process performance. It is also unclear what happens to surface contamination and LPBF-generated surface heterogeneities, such as

---

thermal oxides or material segregation, after reprocessing using such techniques. There is therefore an opportunity available for a process, which can remove near-surface layers without significantly affecting overall powder size or composition. In this study, chemical reprocessing is explored to allow the removal of surface compositional heterogeneity from the powder surface resulting from LPBF. This has been investigated for Cu powder samples that are highly sensitive to oxidation at high-temperature and under ambient conditions [12].

The application of Cu is driven by its thermal and electrical conductivity, where the room temperature electrical conductivity is second only to Ag out of all elements [13]. Coupled with the design freedom associated with AM methods, the excellent heat transfer properties of Cu could allow the fabrication of highly efficient heat exchangers, which could benefit multiple fields of high value manufacturing. However, Cu is extremely sensitive to surface oxidation, especially in situations where moisture cannot completely be excluded from powder feedstocks. This affects powder handling routines prior to LPBF, and the opportunity for powder re-use is greatly limited, given incorporation of surface oxides into the final part will reduce the electrical and thermal properties compared to pure Cu. For these reasons, Cu powder is a useful test case for the principle of chemical reprocessing and oxide removal.

LPBF of Cu is challenged by the interaction of the material and the process, in which the use of Yb-fibre lasers ($\lambda \approx 1070$ nm) dominates due to the relatively low cost and high degree of control over energy delivery. Cu is highly reflective in this spectral region [14], which complicates the initial interaction between the beam and a given powder particle, inhibiting the absorption of energy [15]. This effect is compounded by the high thermal conductivity of Cu, which rapidly draws heat away from the fusion zone. Accordingly, as-built Cu parts often show low density and relatively poor electrical conductivity without further heat treatment [16]. Appropriate parameter selection including high laser powers (>300 W) and substrate preheating can help to improve the density and electrical properties of Cu parts [17], while post build heat treatments can improve electrical conductivity and mechanical properties, particularly in the case of precipitation strengthened Cu-alloys like CuCrZr [18]. High back reflectance onto optical components, like mirrors, within the LPBF system can exceed the laser induced damage threshold [19]. This can ultimately damage the system, especially at high laser powers required to optimise Cu deposition in LPBF.

The optical properties of Cu powders can be improved by adjusting the surface composition and chemistry, for example through deposition of material that is more absorptive at near-IR wavelengths. Chemical methods like immersion plating have been exploited to deposit films of Sn, which has been shown to improve absorptivity and final deposit density and electrical conductivity [20,21]. Physical coating methods like physical vapour deposition (PVD) have been applied to coat Cu powders with CrZr [22] and Zn [23], while controlled thermal oxidation of Cu powders has been shown to improve the build quality of generated parts through increasing the quantity of energy absorbed and transferred to the melt pool [24].

In this study, used LPBF powder is chemically modified to reduce surface oxides, thereby allowing reusability of spent powder. A wet chemical etching process was applied to Cu powder in two supply conditions: virgin (as received) and spent (after LPBF). This Spent Cu powder was collected adjacent to the outlet and is discoloured in comparison to the Virgin Cu powder (Fig. 1b-c).

Wet chemical etching can be carried out under ambient conditions and is scalable to industrial throughputs, for example by flow reactors or fluidised beds. Such chemical processes are therefore potentially cheap and attractive to industrial practitioners. However, etching processes remove material from the powder, and wet chemical processes by their nature may complicate the drying of the powder. Although waste streams containing dissolved metals will be generated during the process, it is important to note that metal-rich filtrates (e.g., Cu) are unlikely to be discarded after use when created in large quantities, where they can be easily recovered. As such, mass loss in this case does not represent the end of the life cycle. In effect, the methodology presented here forms an attempt to 'reset' the surface chemistry of the metal powder, such that surface concentrations of thermal oxides do not enter subsequent builds, interact with the LPBF process, or reduce the quality of the resulting parts. Alternative methods, like exposing powder particles to reducing atmospheres at elevated temperatures has also been shown to successfully reduce surface and interior oxidation in oxygen-sensitive materials like Fe [25]. The reprocessing methodology presented here is a low-energy, surface sensitive route designed to remove oxidation from the surface of spent powder. This route could be applied in conjunction with spheroidisation processes that partially or fully melt the powder such as plasma [11], electron beam [26], and thermal [27] processing that have been shown to improve powder flowability [28].
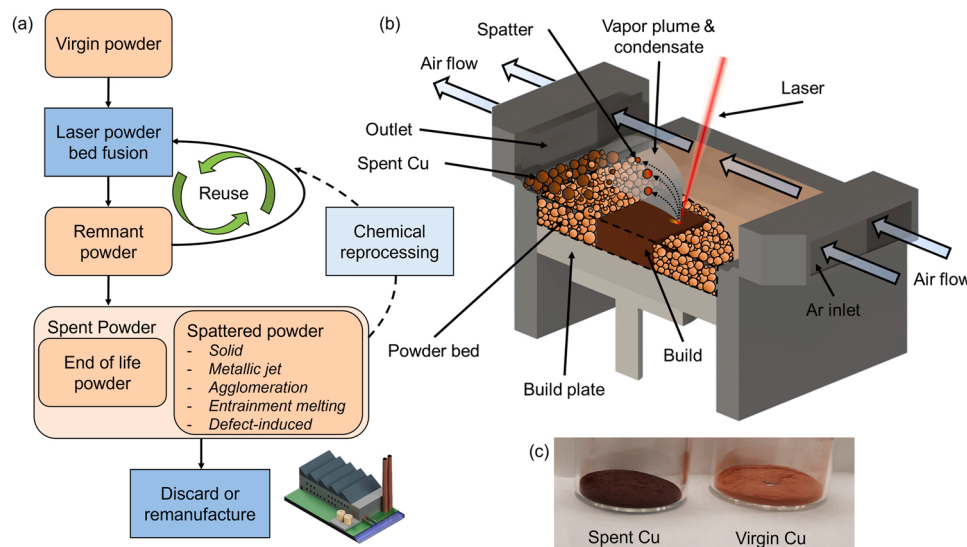
Fig. 1. a) Flow diagram of powder usage in LPBF. Most powder is discarded after a given number of usage cycles as it degrades through mechanisms like spatter and oxidation. b) Schematic of LPBF setup during a build. Spatter and condensates collect around the outlet, driven by the shielding gas stream. c) Photograph of the discoloured Spent Cu collected from adjacent to the outlet in comparison to the Virgin Cu.

2. Methodology

2.1. Materials

Two different initial powder conditions were investigated to characterise the effects of surface composition and morphology after chemical reprocessing. Virgin Cu powder was used (ECKA Granules, Germany, Ø max. 45 μm), along with the same powder after application in LPBF (Spent Cu). Spent Cu powder was supplied from builds used in a previous study [16], collected adjacent to the outlet (Fig. 1b). The Cu powder was collected after 12 build cycles in total. The builds comprised of 5×5×5 mm cubes and 20×20×20 mm lattice structures. This powder is predominantly spatter from the vapor plume, has interacted strongly with the laser and is discoloured (Fig. 1c). Such powder is generally discarded after use. This material was sieved (<45 μm) prior to chemical reprocessing to remove agglomerates.

2.2. Reprocessing

Chemical reprocessing was undertaken in a batchwise manner, using a Nital etchant (5 wt%) prepared from industrial methylated spirits (IMS, 74% Fisher) and nitric acid (69%, Fisher). The dissolution of Cu in dilute nitric acid solutions is expected to follow Eq. (1), while the cupric oxide (CuO), a basic oxide, will dissolve overall following Eq. (2) [22], occurring spontaneously at room temperature.

$$3Cu + 8HNO_3 \rightarrow 3Cu(NO_3)_2 + 2NO + 4H_2O \qquad (1)$$

$$CuO + 2HNO_3 \rightarrow Cu(NO_3)_2 + H_2O \qquad (2)$$
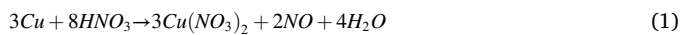
Spent Cu and Virgin Cu powders were subjected to equivalent etching parameters (De-oxidised Cu and Etched Virgin Cu, respectively) to isolate and understand the impact of the prior LPBF oxidation and particle morphology changes on the etching process.

For gravimetric trials, sample sizes 1.40–1.60 g were weighed prior to etching and after recovery. Nital volumes of 20 ml (± 3 ml) were used to etch powder samples. Temperature was measured during etching, where ranges are quoted as the measured temperature at the start and end points of the process. Temperature was modified using a bath setup, controlled with an ice-IMS bath, an ice-water bath, and a hotplate. Sample batches were stirred with Nital for controlled time periods (5, 10, and 20 min), before dilution in IMS to arrest etching. The resulting slurry was then filtered and rinsed with IMS, followed by acetone. Sample batches were then dried before further characterisation.

2.3. LPBF trials and in-situ calorimetry

Single weld seams were deposited onto Cu disc substrates. Cu discs were fabricated by mechanical milling from Cu rod, with a thickness of 0.5 mm, diameter of 10.0 mm, and a 0.1 mm internal recess into which different powders were manually placed prior to LPBF. Discs were degreased with acetone prior to powder placement. Tracks were consolidated from this preplaced powder onto the disc substrates with a commercial LPBF machine (Renishaw AM400), equipped with a pulsed Yb-fibre laser (400 W, λ = 1070 ± 10 nm), spot size 70 μm. While Cu has much better absorptivity in other regions of the spectrum, for example 515 nm [29], near infrared (NIR) wavelengths were applied in this study as they are used in the majority of commercial LPBF apparatus. Substrate discs were fixed onto a purpose built tripod setup, described elsewhere [30], and mounted within the LPBF system. LPBF was undertaken in an Ar atmosphere (<100 ppm O), to reduce in-process oxidation.

6 tracks (6 mm long) were produced on each substrate disc. Incident laser power (400 W) and exposure time (600 μs) were maintained throughout experiments, while two point distances were applied (30 and 60 μm) for effective scan speeds of 50 and 100 mm/s. Three repeats

were performed for each powder sample. Processing parameters were chosen to target melting conditions near the keyhole mode welding regime by reaching the maximum output power of the laser, informed by prior studies [15]. Cu sample discs were subsequently sectioned after LPBF using wire electrical discharge machining, rinsed with acetone, and mounted to characterise cross-sections.

In-situ calorimetry was performed with a purpose-built LPBF machine, equipped with a Yb-fibre laser (600 W, λ = 1070 nm), to understand how surface oxides and their removal affect the LPBF characteristics of these powder samples. The methodology and setup applied to acquire absorptivity data is described in previous studies [15, 31], where absorptivity is the ratio between the energy required to heat the substrate disc to the measured temperature (measured by two K-type thermocouples spot-welded to the disc base) and power transferred by the laser. Cu powder was preplaced into the Cu discs (10 mm diameter, 0.5 mm thickness, 0.05 mm internal recess) and manually spread using a razor blade as a 0.05 mm thick single layer. Incident laser power (540 W) was maintained throughout calorimetry experiments, while three scan speeds (25, 50 and 100 mm/s) were applied. Three repeats were performed for each powder sample.

2.4. Characterisation

Scanning electron microscopy (SEM) was performed using a Zeiss Crossbeam 550 microscope. Energy-dispersive X-ray spectroscopy (EDS) was performed using an Oxford Instruments X-Max80 detector. Pointwise EDS measurements were acquired at controlled acceleration voltage and acquisition time (10 kV, 60 s). X-ray photoelectron spectroscopy (XPS) was performed using a VG Scientific ESCALAB MkII Instrument (Al anode, 12 kV, 20 mA, 10 mm spot size), where all energies are quoted as binding energies. Powder surface chemistry was quantified from survey scans across the binding energy range: 0 – 1200 eV, while high-resolution Cu 2p scans and O 1 s scans were acquired from 928 to 949 eV, and 527 – 537 eV, respectively. Diffuse reflectance measurements were performed on prepared powders using an Agilent Cary 5000 UV–vis–NIR spectrometer (λ = 975 – 1175 nm).

3. Results and discussion

3.1. Surface morphologies

The influence of etching on the powder surface topography was appraised by SE microscopy and diffuse reflectance spectroscopy. Fig. 2 shows powder micro-topography before and after chemical reprocessing (21 – 24 °C, 20 min) for both Virgin and Spent Cu powders. Virgin Cu has a smooth topography that is characteristic of gas-atomised powder (Fig. 2a). Etching Virgin Cu reveals anisotropic facets consistent with the underlying microstructure (Etched Virgin Cu (20 min), Fig. 2b). The surface morphologies of the Spent Cu are complex, where most spent powder particles appear to have a fine nanoscale coating of oxide over the surface (Fig. 2c). However, other oxide morphologies are observed, such as colonies of apparently acicular nanorods shown in Fig. 2c (bottom). The difference between oxide morphologies within the same Spent Cu sample likely results from the heterogeneous thermal cycles experienced by discrete powder particles that comprise this powder. Other processes that may lead to the formation of different oxide morphologies occur within LPBF, including spattering and ejection, as well as direct irradiation and conduction, challenge our understanding of the thermal history of the powder bed in LPBF. The SE micrograph of the corresponding De-oxidised Cu powder indicates the removal of the defined oxide layers that are observed on the Spent Cu (Fig. 2d). Defined facets are revealed, like the Virgin Cu sample etched at the same temperature (Fig. 2b). No oxide layers or nanorod colonies are present on the De-oxidised powder, and their presence on the initial spent powder does not appear to impact the material removal and development of etch facets on the powder surface.
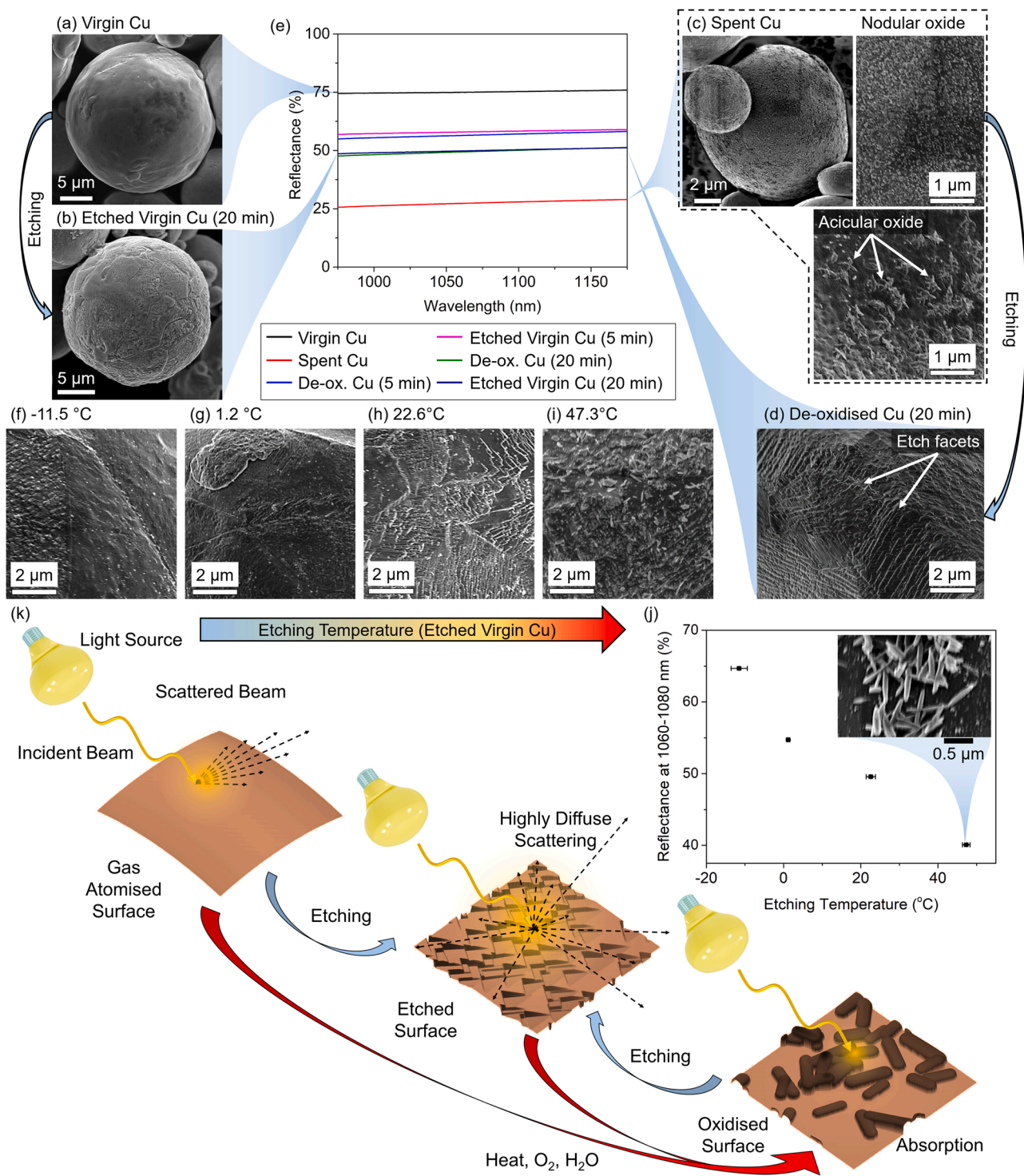
Fig. 2. Chemical reprocessing alters the surface morphology and chemistry. SE micrographs of: (a) Virgin Cu, (b) Etched Virgin Cu (20 min), (c) Spent Cu, showing different oxide layer morphologies, (d) De-oxidised Cu (20 min). (e) Reflectance spectra across the NIR range (975 – 1175 nm). SE micrographs of Virgin Cu samples etched at different temperatures. (f) – 11.5 °C, (g) 1.1 °C, (h) 22.6 °C, (i) 47.3 °C. Surfaces roughen on increasing etching temperature. (j) Diffuse reflectance for these etch samples. (k) Mechanism of incident light interaction with a particle surface in gas atomised, etched, and oxidised conditions. Where topography length scale approaches incident wavelength, highly diffuse scattering is expected.

The surface topography and chemistry, specifically the presence of etch facets and oxidation, dictate the interaction of the powder with light. The caveat being that rapid melting under irradiation during LPBF mean that minor differences in surface topography are unlikely be retained beyond the initial excitation. Nevertheless, differences in absorptivity between powders may drive differences in the initial melting

phase; this may be beneficial given the high reflectance of Cu. As such, diffuse reflectance was appraised for Virgin, Spent, and room temperature (21 – 24 °C) etched powders (5 and 20 min) across the NIR spectral region (975 – 1175 nm) around the laser wavelength, shown in Fig. 2e.

In the region corresponding to the Yb-fibre laser wavelength (≈1070 nm), reflectance is relatively high (74.9%) for Virgin Cu. Spent

Cu showed a significant reduction in reflectivity at 1070 nm (28.9%), which is indicative of a difference in surface chemistry and topography resulting from the LPBF process, likely due to surface oxidation present in the spent powder (Fig. 2c-d). The etched powders possess similar reflectance at 1070 nm regardless of the initial supply condition both after 5 min of etching (56.6% and 58.0% for the De-oxidised and Etched Virgin samples, respectively), and after 20 min of etching (49.6% and 49.9% for the De-oxidised and Etched Virgin samples, respectively), at room temperature (21 – 24 °C). This indicates similar surface conditions result from equivalent etching steps and are independent of the nature or extent of LPBF-induced surface oxidation. All spectra are stable within this range, however the measured absolute reflectance value is reduced in comparison to bulk Cu (>95% reflectance at 1070 nm at 300 K [32]), likely due to the particulate nature of the sample, where the high powder surface area to volume ratio implies native Cu-oxides present under ambient conditions will interact more strongly with the incident beam.

Given reaction kinetics are dictated by temperature as described by the Arrhenius relationship, the effect of bath temperature under near-ambient conditions (<50 °C) on etch surface development was appraised (20 min etching). The surfaces of Virgin Cu etched at different temperatures were assessed by SE microscopy (Fig. 2f-i). The results show a difference in topography after etching when compared with Virgin Cu (Fig. 2a), characterised by facets. Topography appears to change with etching temperature, likely attributed to an increase in material removal. In this case, the greater the etching temperature, the greater the apparent prominence of the etch facets. These are revealed even at the lowest etching temperatures studied (Fig. 2f-g). However, apparent surface oxidation is observed in the high temperature (mean 47.3 °C) etch sample (Fig. 2i). Nevertheless, even at high etching temperatures, the revealed topography is more complex than the gas-atomised initial state.

The apparent prominence of etch facets on the powder particles correlates with the incident light wavelength in LPBF using a Yb-fibre laser. Diffuse reflectance in this region (1060 – 1080 nm) is shown in Fig. 2j and is dependent on etching temperature. Compared with the Virgin Cu (74.9%), diffuse reflectance decreases even under cold etching conditions (64.7% at −11.5 °C and 54.7% at 1.2 °C), while heating further decreases reflectance (40.1% at 47.3 °C).

The decrease in measured diffuse reflectance on etching likely results from the enhanced scattering of light from the revealed etch facets (Fig. 2k). While there will be a specular reflective component resulting from groups of similarly oriented etch facets within a given grain, each powder particle is composed of multiple discrete grains. In addition, spherical powder shapes will further complicate the final etch facet geometry as, for an anisotropic etch, the geometry is dependent on the orientation of the slow-etch directions relative to the dissolution front. For a given crystalline grain within a powder particle, this changes with different relative angular rotations around the powder surface. Cu-oxide phases, which are prominent in the Spent Cu powder and heated etched powder (Fig. 2j, inset), readily absorb light at this wavelength in comparison to metallic Cu [24]. As such, it is challenging to isolate the effects of surface chemistry and topography on the diffuse reflectance.

3.2. Surface chemistry

Both surface chemistry and topography affect the interaction of incident light with the sample. The level of surface oxidation on the powders etched at room temperature (21 – 24 °C, Table 1) was assessed with XPS and EDS. EDS indicates a high degree of surface oxidation on the Spent Cu sample (O Kα = 17.5 ± 7.0 at%) compared with the Virgin Cu sample (O Kα = 2.1 ± 0.8 at%), correlating with the SEM micrographs showing surface oxide crystals (Fig. 2c). The EDS data indicates the surface O concentration of the two etched powders (20 min) falls within the error ranges of the Virgin Cu sample (De-oxidised Cu: O Kα = 2.7 ± 0.7 at%, Etched Virgin Cu O Kα = 1.8 ± 0.9 at%). The XPS data also shows a reduction in O concentration on etching, for both samples,

Table 1
Quantitative EDS and XPS data for Cu powders (21 – 24 °C) (at%).

Element	Virgin	Spent	Etched Virgin (20 min)	De-oxidised (20 min)
O (EDS)	2.13 (± 0.75)	17.50 (± 6.92)	1.84 (± 0.86)	2.71 (± 0.70)
O (XPS)	53.40 (± 1.04)	38.01 (± 0.75)	29.95 (± 0.79)	27.36 (± 0.78)
Cu (XPS)	20.36 (± 0.82)	30.40 (± 0.68)	31.71 (± 0.91)	31.32 (± 0.88)

although initial O concentration in the Virgin Cu (53.4 ± 1.4 at%) is greater than for the Spent Cu (38.0 ± 0.8 at%).

The results indicate a discrepancy between EDS and XPS that is related to the sampling depths of the respective methods and the surface chemistry of each powder sample. The sampling depth in EDS correlates to the penetration depth of the primary electron beam, which may be on the scale of 1 – 2 μm in pure Cu for a 10 kV beam, and likely deeper through a surface oxide layer. EDS is therefore sampling the metal below the oxide layer. This appears to indicate a thicker oxidised layer in the Spent Cu sample, extending further into the sampling depth of the electron beam in EDS analysis, thereby resulting in a greater oxygen signal. In contrast, photoelectrons in XPS are liberated from the near surface (<20 nm) and can provide extremely surface-sensitive chemical information. Both techniques indicate a reduction in surface O concentration upon etching, and a convergence towards the same O concentration regardless of the initial powder condition.

From the XPS spectra, the powder surface chemistry can be elucidated. Fig. 3 shows the high-resolution XPS spectra of the powder samples in the spectral region corresponding to the Cu 2p 3/2 (928 – 949 eV) and O 1 s bands (527 – 537 eV), along with the Gaussian fitting for each XPS curve (dashed curves). Positions of fitted peaks are tabulated in Table 2 and Table 3.

For both the Virgin and Spent Cu (Fig. 3a-b, black series), the specific Cu chemical environment is dominated by Cu(II), indicated by the presence of shake-up satellite features accompanying the main 2p 3/2 peak. This indicates the presence of Cu(II) species, such as CuO, or hydrated Cu(II) species like $Cu(OH)_2$, both of which are understood to form on Cu under ambient conditions. These form as components of the native oxide layer after more rapid formation of initial Cu(I) species like Cu_2O [33]. The relatively high binding energies of the Cu 2p 3/2 peak for both Virgin and Spent Cu (>934 eV) could suggest $Cu(OH)_2$ [34]. Shake-up features are stronger in the case of the Spent Cu powder (Fig. 3a), comparing the ratio of these satellites to the main peak contributions for both un-etched powders (Virgin Cu: 16.4%, Spent Cu: 34.8%). Thus it is reasonable to suggest a greater surface Cu(II) concentration in the Spent Cu. In the case of Virgin Cu, the main peak is also asymmetric, indicative of more complex surface chemistry than the Spent Cu. While there is a broad peak corresponding to a Cu(II) chemical environment (934.5 eV), there is also a downshifted peak (932.7 eV), which likely corresponds to metallic Cu(0) or Cu(I). The presence of Cu(I) cannot be excluded given the similar energies of these expected peaks in XPS, although it may be expected at lower binding energy (e.g. ≈932.18 eV [35]). Upon etching, the Cu(II)-dominated surface chemistry is removed, evidenced by the absence of satellite features and a narrowing and sharpening of the main peaks (Fig. 3a-b, red series). Additionally, the binding energies of the 2p 3/2 main peaks are downshifted in energy (Virgin Cu: 932.8 eV, Spent Cu: 932.6 eV) upon etching. Again, this indicates the presence of near-surface metallic Cu or Cu(I). Exposed Cu(0) will be rapidly oxidised to Cu(I) under ambient conditions [36].

While O 1 s peaks are challenging to interpret given the superimposition of multiple possible excitations, the Virgin Cu and Spent Cu powders show different oxygen chemical environments (Fig. 3c-d, black series), the latter showing strong asymmetry. For example, the sharp low energy peak (529.9 eV) in the Spent Cu likely corresponds to Cu(II)-bonded lattice O [34]. Referring to the Cu 2p analysis for this
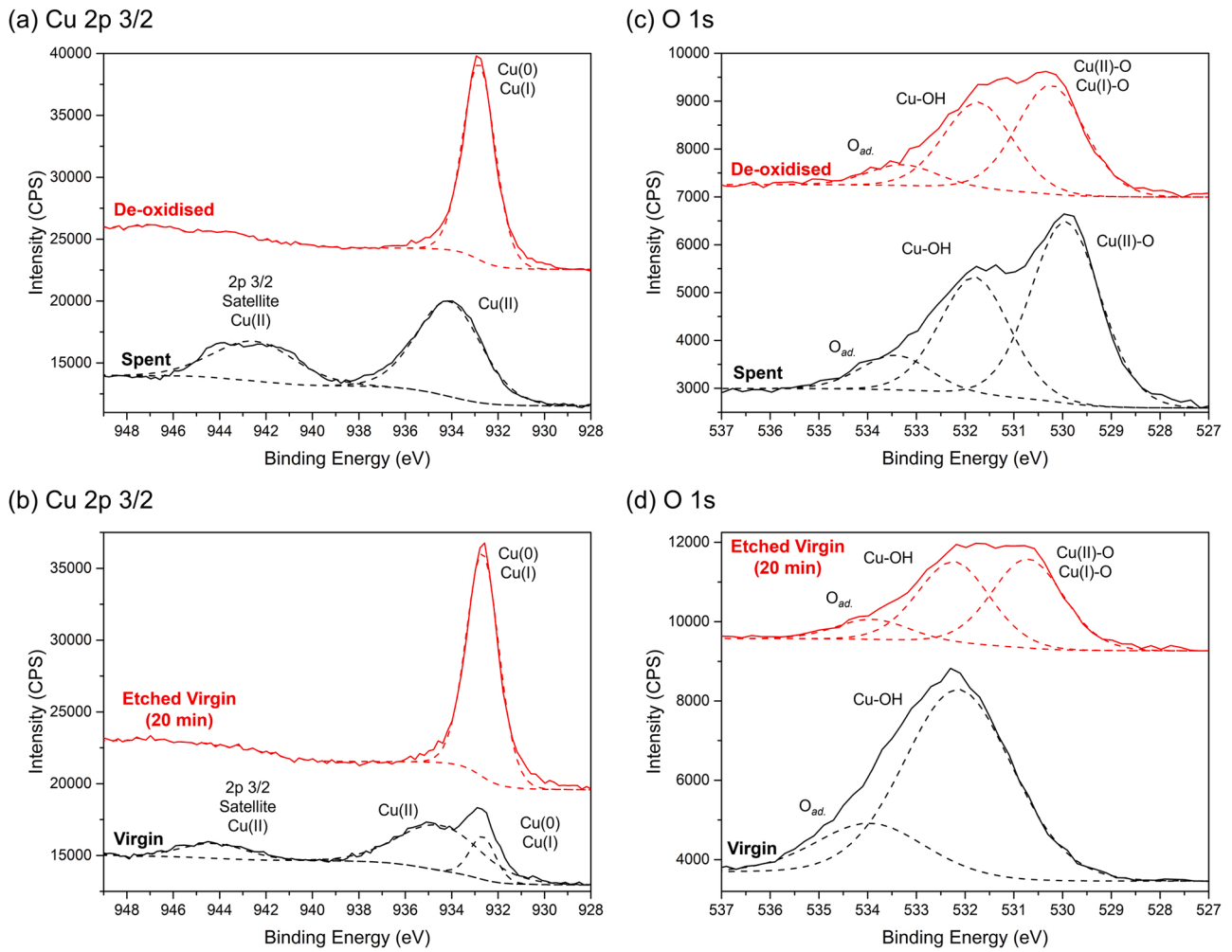
Fig. 3. High-resolution XPS spectra for the powders: Virgin, Spent, De-oxidised (20 min), and Etched Virgin (20 min). a-b) Cu 2p 3/2 region (928–949 eV), and c-d) O 1 s region (527–537 eV). Black series are the powder samples prior to etching and red series after etching.
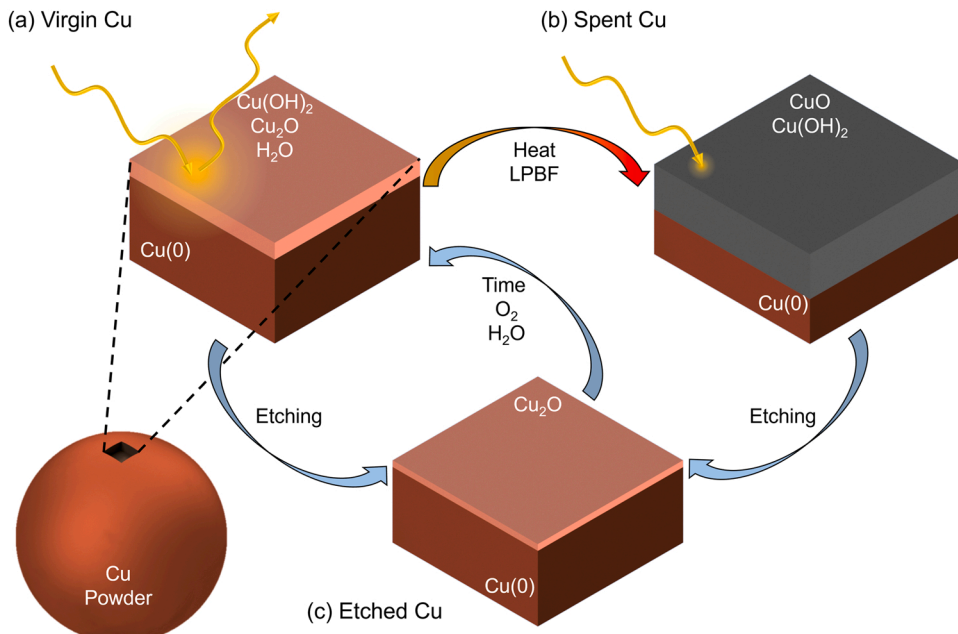
Fig. 4. Thermal history and exposure to ambient conditions affect powder surface chemistry. a) Virgin Cu with a thin mixed layer consisting of Cu_2O and $Cu(OH)_2$. b) Laser interaction and heating $> 150\,°C$ during LPBF decomposes the $Cu(OH)_2$ into CuO, where diffusion of surface O into the particle increases the oxide layer thickness. c) Etching removes top surface layers, leaving a thin film of native Cu_2O under ambient conditions. Exposure to humidity over time will return the surface state to a).

Table 2

XPS possible identifications, peak positions, and satellite to main peak ratios for the Cu 2p 3/2 peaks.

Cu 2p 3/2 Species	Unit	Spent	Virgin	De-oxidised (20 min)	Etched Virgin (20 min)
Binding Energy: Cu(0) or Cu(I)	eV	–	932.7	932.8	932.7
Binding Energy: Cu(II)	eV	934.1	934.5	–	–
Binding Energy: Satellite Cu(II)	eV	942.5	944.2	–	–
Ratio: Satellite/ Main peaks	%	34.8	16.7	–	–

Table 3

XPS possible identifications, peak positions, and satellite to main peak ratios for the O 1 s peaks.

O 1 s Species	Unit	Spent	Virgin	De-oxidised (20 min)	Etched Virgin (20 min)
Binding Energy: Possible Cu(II)-O	eV	529.9	–	–	–
Binding Energy: Possible Cu(I)-O	eV	–	–	530.8	530.7
Binding Energy: Possible Cu-OH	eV	531.8	531.7	532.3	532.2
Binding Energy: O_{ads}	eV	533.4	533.3	533.9	533.9
Ratio: O_{ads} to other O 1 s	%	10.4	27.6	9.7	10.6

powder (Fig. 3a, black series), this is strong evidence of near-surface CuO. The Virgin Cu powder does not show this lattice bonded O peak, despite the presence of Cu(II)-species, shown in (Fig. 3b, black series). This suggests a mixed layer in the Virgin Cu powder comprising of alternate Cu(II) species, for example $Cu(OH)_2$, as well as Cu(I) species like Cu_2O. After etching, both De-Oxidised and Etched Virgin Cu powders have a similar low energy peak (530.7 – 530.8 eV), at a higher binding energy than the Cu(II)-O lattice bonded O peak in the Spent Cu powder (529.9 eV). This could indicate the presence of Cu(I)-O lattice bonded O, present in Cu_2O. Furthermore, all powder samples indicate the presence of a broad peak (531.8 – 532.3 eV) that could be indicative of surface Cu-OH or adsorbed organic material. All analysed powder samples show a high binding energy peak (533.3 – 533.9 eV) that corresponds to weakly adsorbed O-species [37], for example H_2O.

It is likely that the surface layers on the Virgin Cu powder are a hydrated mixture of $Cu(OH)_2$ and possibly Cu_2O, while the Spent Cu powder appears to be mainly Cu(II), with evidence for both CuO and Cu(OH)$_2$ (Fig. 4). This is consistent with observations that $Cu(OH)_2$ is a metastable phase that will decompose to CuO at relatively low temperatures ($\approx$150 °C [38]). These are consistent with the powder bed preheating temperatures applied during prior LPBF (170 °C [15]), from which Spent Cu powder was recovered. A greater surface concentration of $Cu(OH)_2$ and adsorbed moisture on the Virgin Cu could explain the higher O concentration (XPS, Table 1), compared with the Spent Cu, despite the thinner oxidised layer, indicated by both the EDS and SEM (Fig. 2). Etching removes these Cu(II) layers from the powder surface, likely exposing metallic Cu initially. This will rapidly oxidise to a thin Cu_2O film under ambient conditions, where exposure to humidity is known to increase oxidation rates of Cu powders [12]. In this context, both EDS and XPS analyses indicate a reduction in the oxide level, and an effective chemical reduction of this surface oxidised layer from Cu(II), while equivalent surface chemistries are recorded for both De-oxidised and Etched Virgin Cu powders, regardless of initial surface chemistry.

3.3. Process control

Etching yields and particle size distributions were appraised using the batch setup. Prior to this, further control samples (No Etch Control) were prepared by stirring powder with IMS (without Nital) and then recovering the powder by the same filtration and drying steps as the etched powders. This was carried out to determine the extent to which powder was lost during handling and filtration steps, where results indicate yields of 94.9% ($\pm$ 0.1%) with the setup used in this study. Using the same setup, recovered yields will likely be higher for i) larger powder sizes that will be less prone to losses through filtration and handling, and ii) larger sample masses. It is expected that handling and filtration losses would be greatly reduced on process scale-up.

The kinetics of Cu powder dissolution in nitric acid solutions have been previously investigated, intuitively demonstrating the reaction rate dependence on temperature, particle size, agitation, and acid concentration [39]. The effect of etchant temperature on yield for Virgin Cu powder in this setup was appraised after etching for 20 min (Fig. 5a). The results indicate material removal at all temperatures, showing a decrease in yield with temperature. A high yield (92.3%) was recovered at the lowest temperature tested (mean −11.5 °C) when compared with the no-etch control sample, indicating limited etching. Conversely, at
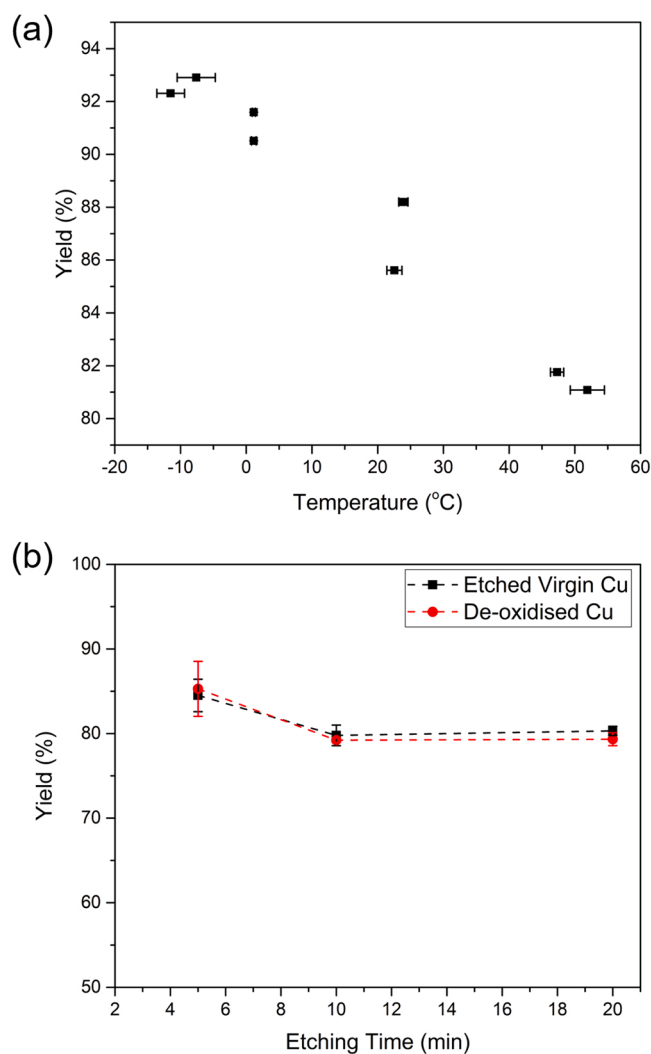
Fig. 5. (a) The relationship between temperature and etching yield for the virgin Cu powder. (b) Powder yields for all samples (etch temperature 21–24 °C). Error bars are the standard deviation from the mean of three discrete etching trials.

the highest temperature tested (mean 51.9 °C), a yield of 81.1% was recovered. The rate of the etching reaction is accelerated by temperature elevation partially because the mass transport of reactants and products to and away from the particle surface is enhanced. This is an important consideration for increasing scalability, where faster rates will reduce processing times. High temperature processing over extended timescales might likely over-etch the powder and remove more of the pristine underlying metal. This is undesirable, however the Cu-rich filtrate cannot be considered a waste product when such processing methods are scaled up to industrial levels.

The effect of etching time on recovered mass was appraised at fixed temperatures (21–24 °C). The returned yields indicate material removal (79–85%) for all trials in this study, shown in Fig. 5c. No change in yield

is observed for etching times greater than 10 min, which indicates self-limitation of the etching reaction between 5 and 10 min within this temperature range. No difference in etching rates between the Virgin Cu powder and the Spent Cu powder is observed under these etching conditions.

Powder sizes were assessed before and after chemical reprocessing. Particle size distributions for these samples are shown in Fig. 6a for Virgin Cu, Etched Virgin Cu (20 min), and a secondary control powder (No Etch Control), subjected to equivalent powder handling and recovery after immersion in IMS (without nitric acid). This was undertaken to isolate the effect of powder handling on the final particle size from the etching routine. Fig. 6b shows the size distributions for Spent Cu and De-oxidised Cu (20 min etch). SE micrographs are shown for
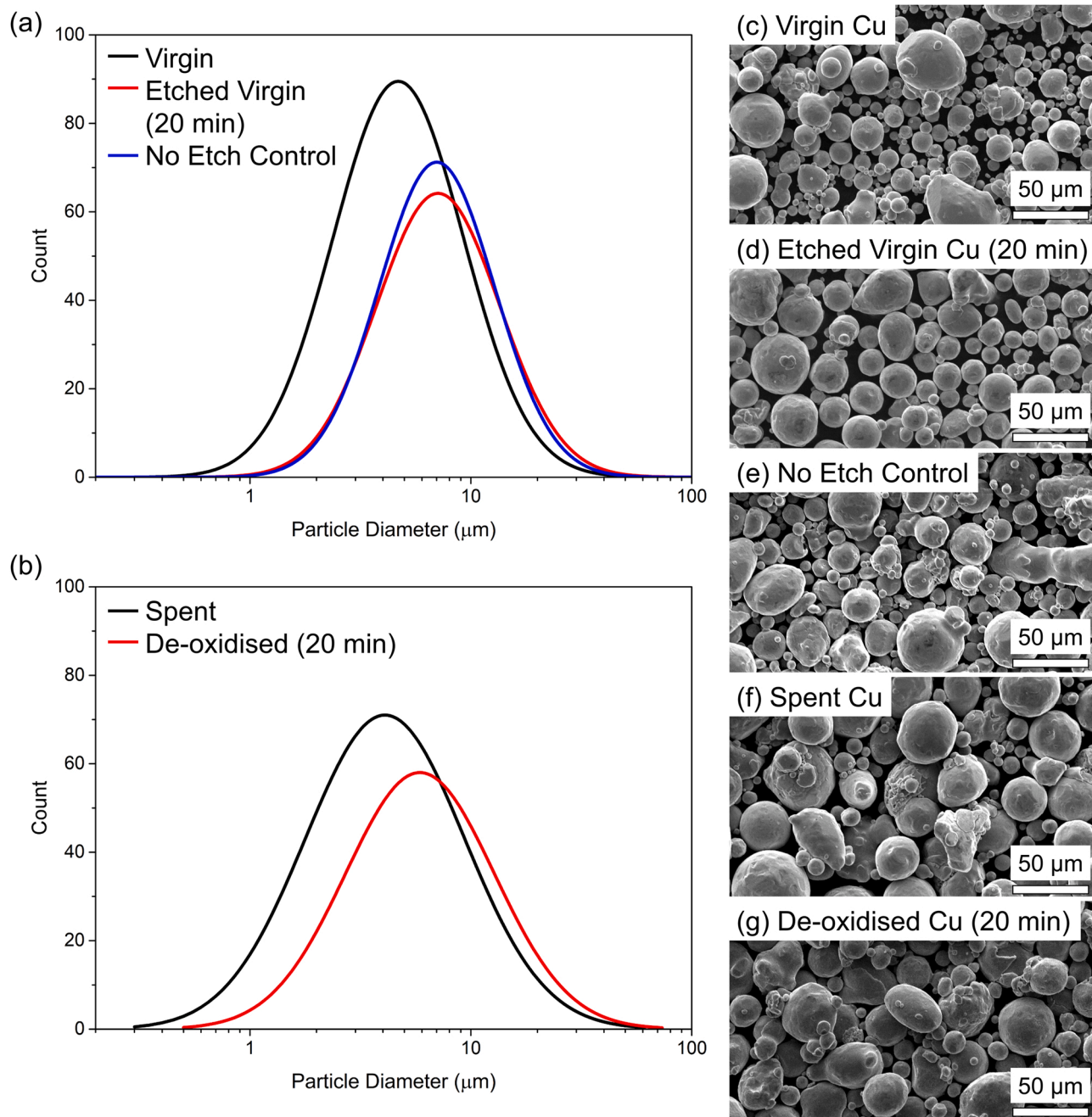
Fig. 6. Particle size distributions for a) Virgin Cu, Etch Control Cu (20 min) and No Etch Control Cu, b) Spent Cu and De-oxidised Cu (20 min). Powder handling with the etching setup reduces the number of fine particles (<5 µm). Curves are the lognormal distribution of the data. Bin size 3 µm. Scanning electron micrographs of the surface of Cu powder particles in different conditions: c) Virgin Cu, d) Etched Virgin Cu (20 min), e) No Etch Control, f) Spent Cu, g) De-oxidised Cu (20 min).

each of these powders (Fig. 6c-g).

Comparing the Virgin Cu (D50: 7.3 µm, mean: 9.4 µm) and the Spent Cu (D50: 7.9 µm, mean: 11.6 µm), the size distribution is marginally skewed towards larger particle diameters after LPBF, due to agglomerates of spatter particles and partially fused regions shown in the micrographs. The size distribution changes upon etching, resulting from a reduction in the fraction of very fine particles (<5 µm diameter). This is mainly caused by losses through powder handling (from air extraction during preparation, and filtration and drying steps), rather than the total dissolution of these finer particles. This is shown by the similar size distributions for the Etched Virgin Cu (D50: 11.3 µm, mean: 12.8 µm) and the No Etch Control sample (D50: 9.6 µm, mean: 12.0 µm) in Fig. 6a. The same effect of fine powder removal is observed in the De-oxidised Cu (D50: 10.6 µm, mean: 14.3 µm), shown in Fig. 6b. While changes to the particle size distribution may be undesirable given the potential changes to powder flowability, finer powder particle losses will be significantly reduced within a scaled-up process, rather than the manual batch etching methodology followed in this study.

3.4. LPBF behaviour

Single track features were fabricated using a Renishaw AM400 LPBF machine from the different powders (Section 2.3). SE micrographs of the top surfaces of tracks deposited at 100 mm/s are shown in Fig. 7a-d for the Spent Cu, De-oxidised Cu (20 min), Virgin Cu, and Etched Virgin Cu (20 min), respectively. In the case of the Spent Cu, some surface porosity is visible (Fig. 7e), which is not apparent to the same extent in the other tracks (Fig. 7g-h), all of which display similar track morphologies. Apparent track width in this experiment is sensitive to the manual powder application step onto the disc and denudation from adjacent tracks, in addition to differences in processability that might arise from differences in absorptivity.

Higher magnification micrographs of surface defects in the Spent Cu tracks are shown in Fig. 8. For example, closely grouped surface pores in Fig. 8a could be indicative of subsurface porosity networks, likely caused by gassing of the oxide-rich surface layer of the Spent Cu powder. In addition, some evidence of intergranular solidification cracking is shown in the backscatter electron (BSE) micrograph in Fig. 8b. This could be related to the possible segregation of oxide-rich phases as they are rejected from the solidifying melt, or float above it, creating relatively brittle regions that could be susceptible to cracking upon the development of cooling-induced tensile stresses. This is supported by the observation of apparently columnar dendritic surface features alongside the crack, and independently in Fig. 8c.

Deposited tracks were sectioned to observe defects and microstructures in the interior, firstly by polishing and using high contrast in optical imaging, and secondly by chemically etching these cross sections (Fig. 9). Optical micrographs of the tracks fabricated at 50 mm/s from the Spent Cu powder (Fig. 9a) show extensive porosity, indicative of significant degassing and vaporisation of material within LPBF. Chemical reprocessing of Spent Cu is shown to drastically reduce this porosity and enhance the apparent density of the fabricated tracks (De-oxidised Cu, Fig. 9b), where the level of porosity is more consistent with tracks fabricated from Virgin Cu (Fig. 9c) and the Etched Virgin Cu (Fig. 9d). This indicates that the chemical reprocessing step has generally reduced this oxide and contamination layer, the decomposition of which during LPBF appears to result in the formation of extensive porosity shown in Fig. 9a. While these parameters (50 mm/s, 400 W) generally lead to keyhole-type melting in agreement with prior studies [15], shown in the corresponding micrographs after etching (Fig. 9e-h), this appears to be partially disrupted when fabricating tracks from the Spent Cu powder (Fig. 9e). Tracks formed at this parameter in other powders instead display evidence of relatively deep keyholes, in some cases penetrating the disc, along with relatively large columnar grain growth that is broadly typical of LPBF deposits in this operational mode.

High levels of porosity are also observed in tracks fabricated from Spent Cu at the higher scan speed (100 mm/s) (Fig. 9i), with a reduction in pore density after chemical reprocessing (Fig. 9j). Apparent density becomes more consistent with that observed in the Virgin Cu and Etched Virgin Cu tracks (Fig. 9k-l). The corresponding etched surface micrographs for these tracks generally indicate conductive mode melting (Fig. 9m-p), evidenced by limited melt pool-substrate mixing, poor wetting, and limited melt pool depth into the disc. Finer and more equiaxed grains in this mode suggest faster cooling rates, where faster freezing will likely lead to the poor apparent interfacial adhesion. It is likely that the extensive networks of pores throughout the deposits fabricated from the Spent Cu powder will detrimentally affect both the mechanical and functional properties (thermal and electrical conductivity) of the deposit in comparison to the Virgin Cu and the De-oxidised Cu tracks.

Fig. 10a shows a BSE micrograph of a large (Ø ≈100 µm) cross-sectioned pore within a track deposited at 50 mm/s from Spent Cu powder. Within the pore, there are annular ring formations consistent with those expected from recoil pressures. These may be associated with the rapid thermal decomposition of oxide and hydroxide-rich surface layers into water vapour and free O_2. Vaporisation would lead to a rapid volumetric expansion caused by both the phase change and thermal expansion. The darker contrast inside of the pore visible in BSE

Spent Cu	De-oxidised Cu	Virgin Cu	Etched Virgin Cu
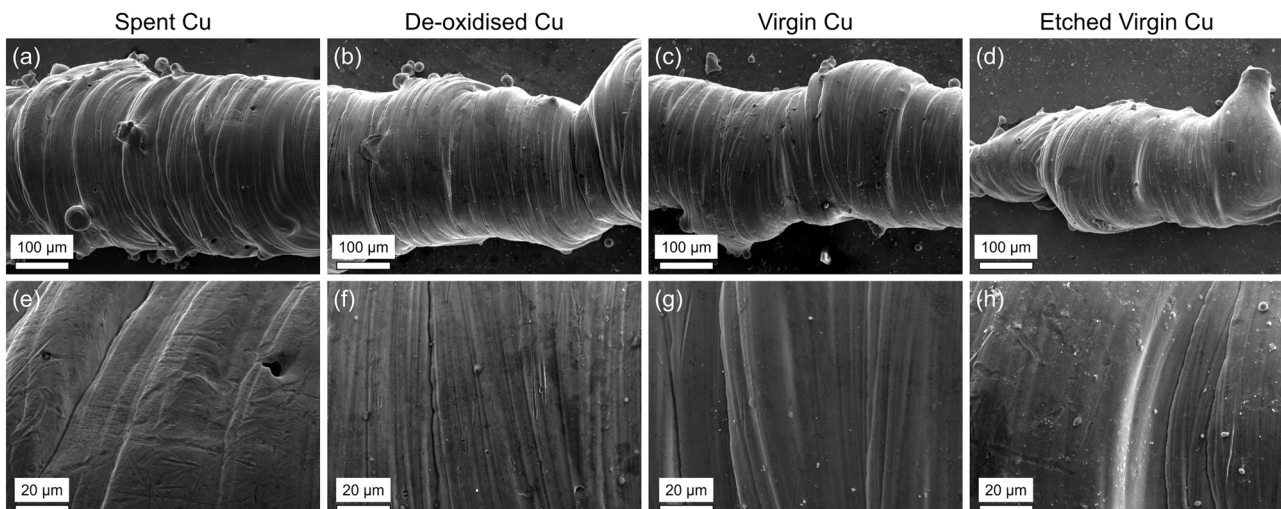
Fig. 7. SE micrographs of tracks deposited at 100 mm/s scan speed. a,e) Spent Cu, b,f) De-oxidised Cu (20 min), c,g) Virgin Cu, d,h) Etch Control Cu (20 min).
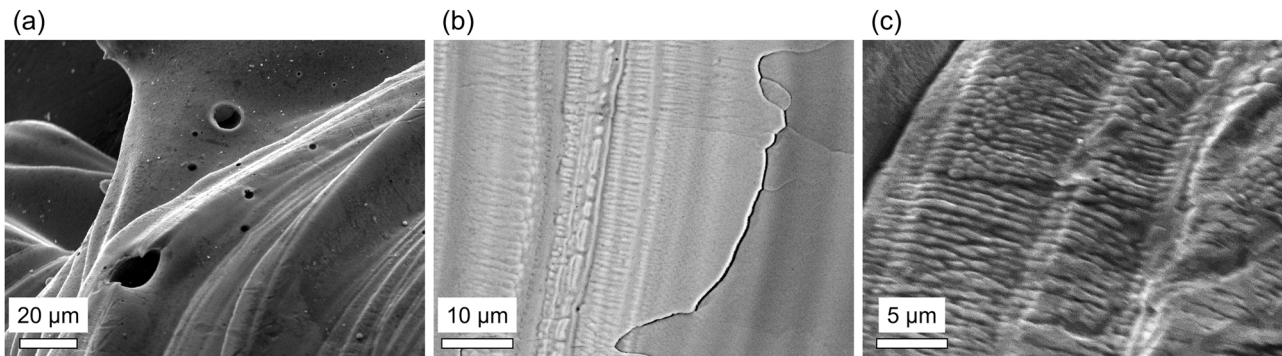
Fig. 8. Surface defects in Spent Cu tracks. a) Closely grouped surface pores, b) BSE micrograph of possible solidification cracking and columnar dendritic formation at the surface, c) high-magnification SE micrograph of surface micro-topography from a dendritic surface region.
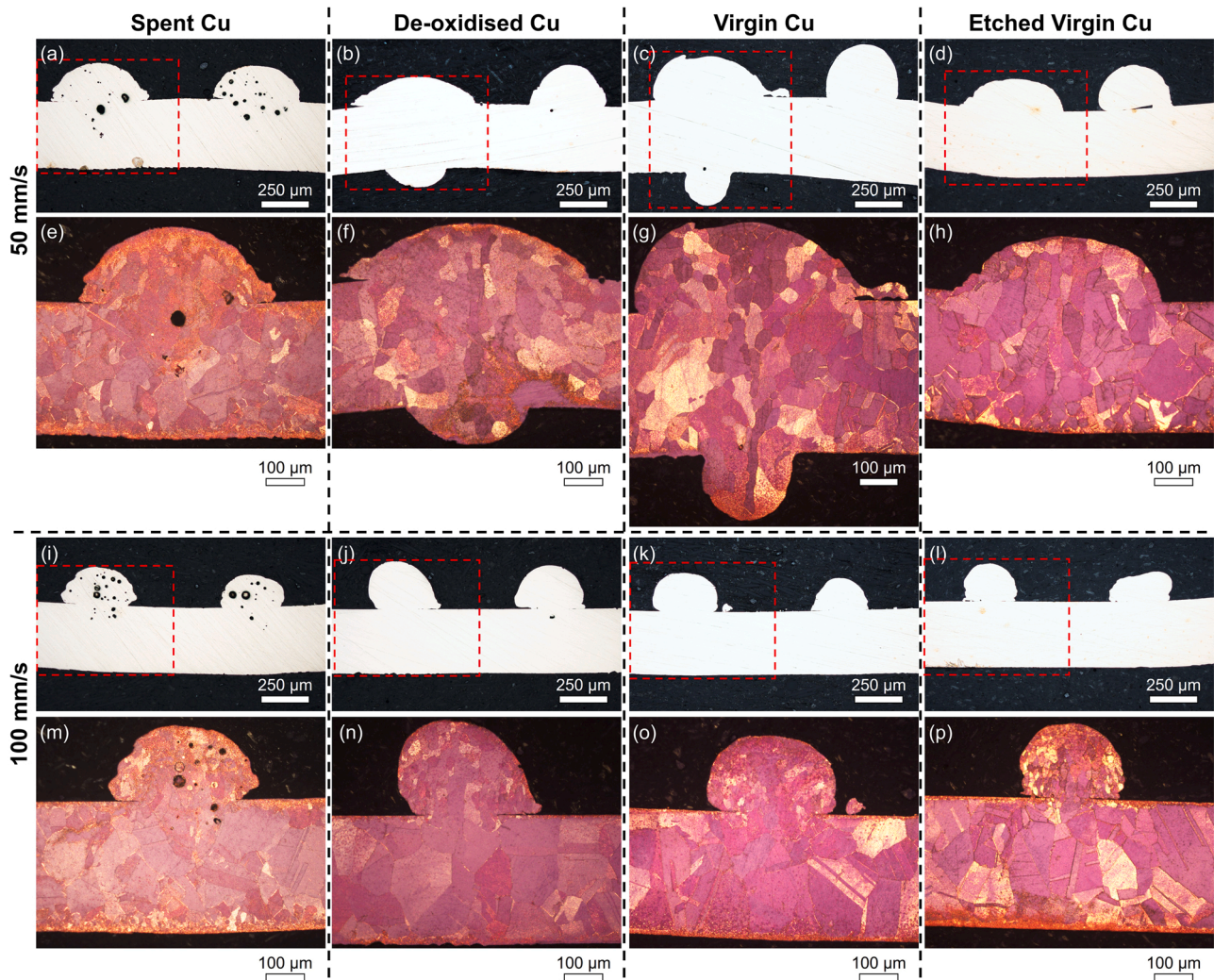
Fig. 9. Cross sections of deposited tracks processed with different powder types. High contrast optical micrographs processed at 50 mm/s. Tracks fabricated from: a) Spent Cu, b) De-oxidised Cu, c) Virgin Cu, d) Etched Virgin Cu. e-h) Etched micrographs for the corresponding powders deposited at 50 mm/s. i-l) High contrast optical micrographs of track sections processed at 100 mm/s for the same powders, and m-p) the same tracks after chemical etching.

microscopy indicates the presence of lower density phases such as oxides on the interior surface. These could occur through the condensation or formation from trapped water vapour upon track cooling. O concentration was appraised by a point-wise EDS line scan across the sectioned pore (Fig. 10b). spectral acquisition points *I-XII* are labelled in Fig. 10a. O concentration is greater within the pore than the track bulk area,

especially where the electron beam is sampling greater volumes of the interior surface, for example at the pore edges. This is consistent with the presence of an oxidised layer thinner than the electron penetration depth ($\approx$2 μm in Cu at 10 kV).

In-situ calorimetry was performed on the powder samples by depositing single tracks (540 W) using the purpose-built setup described
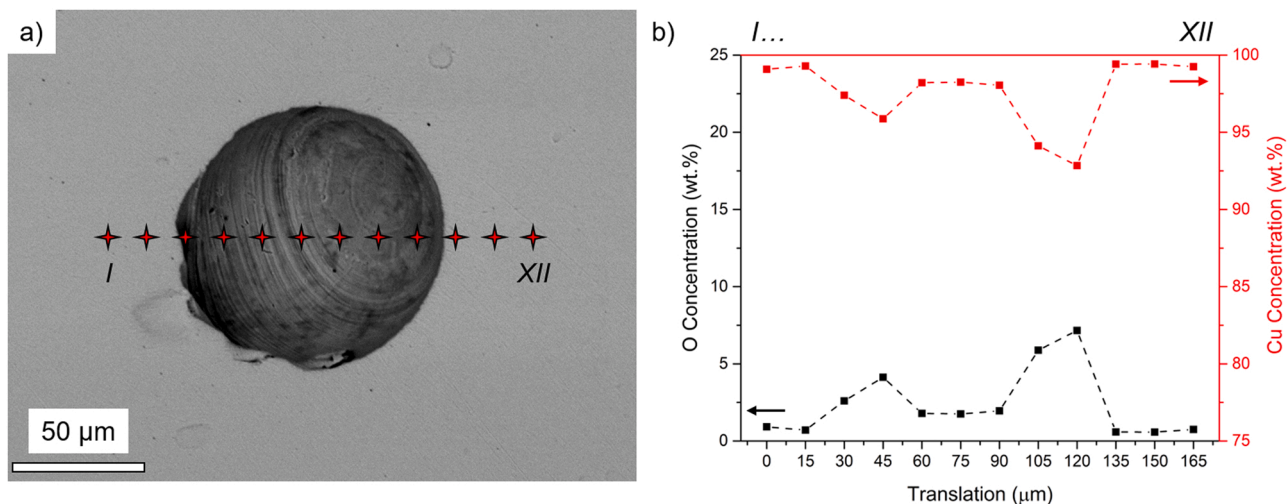
Fig. 10. Large-scale pores are oxygen rich. a) BSE electron micrograph of a cross sectioned large pore in the spent powder track (50 mm/s), showing EDS linescan acquisition points. b) EDS linescan, showing O localisation within the pore.

in Section 2.4 to further understand the in-process response of powder surface modification. Despite the lower diffuse reflectance of the Spent Cu powder (Fig. 2e), the absorptivity in LPBF appears to increase at the tested parameters after surface de-oxidation (Fig. 11). Indeed, the Spent Cu powder shows the lowest absorptivity across the range of scan speeds, despite having the lowest nominal diffuse reflectance of the powder samples tested in this study. Given the significant porosity visible in the cross sections of the tracks deposited with Spent Cu (Fig. 9a, i), this absorptivity drop might be related to the vaporisation of the thicker surface oxide and hydroxide layers in this sample. Here, vaporisation phenomena, including the latent heat of vaporisation, will provide an additional energy sink to transfer heat from the fusion zone. Furthermore, enhanced vaporisation would scatter the incident beam, leading to a reduced interaction with the powder. Both phenomena could lead to the observed drop in absorptivity. Etching this powder appears to increase measured absorptivity across the process parameters tested, likely due to the removal of most of this thick oxide layer present in the Spent Cu. The Virgin Cu and Etched Virgin Cu show similar absorptivity at the lower scan speeds (25 and 50 mm/s), while the absorptivity of the Etched Virgin Cu is greater at the fastest scan speed tested (100 mm/s). This could be a result of the apparent thinning of the

native oxide/hydroxide layer on etching, shown in the complementary EDS and XPS results (Table 1). This would reduce the amount of water vapour released during subsequent LPBF and therefore could reduce vaporisation as a route through which heat is transferred from the melt pool.

3.5. Perspectives

Although Cu is widely applied in heat transfer applications, to which the geometric freedom afforded by LPBF could be exploited to significant advantage, other engineering materials like stainless steels, Ti-alloys, Al-alloys, and Ni-alloys are the subject of more prolific investigation as LPBF feedstocks. Within LPBF, these alloys degrade via additional mechanisms like metallurgical transformations and thermal segregation [2,40], as well as oxidation. In the case of Ti-alloys, incorporation of surface oxides has recently been shown to decrease mechanical properties in test specimens [41]. Therefore, powder degradation through cyclic processing therefore remains a key consideration in LPBF and will continue as alloys are adapted specifically for use in LPBF and material complexity increases [42]. Despite the higher complexity of these materials systems, similar ambient-condition chemical reprocessing and etching steps can be applied to all these materials. Accordingly, the methodology developed here is likely applicable towards most major engineering alloy systems and can readily be scaled up. Considering practical aspects, changes to the microscale surface morphologies of the reprocessed powder particles (etch facets) might alter how they interact under dynamic conditions, which may affect flowability and packing density. This could ultimately influence final part quality and remains the subject of ongoing study.

4. Conclusions

In this study, chemical reprocessing has been introduced as a surface sensitive and low energy (ambient and near-ambient) method through which the surface chemistry of Cu powders can be 'reset', and the topography modulated. The dependence of the etching response on the powder topography, morphology, and chemistry on etchant temperature and time has been assessed. It has been shown that surface oxygen concentrations can be successfully reduced and for both Spent Cu powder, previously applied in LPBF and Virgin Cu powder. This has been demonstrated with both EDS and XPS spectroscopic methods.

Furthermore, the mechanism of Cu powder degradation during LPBF has been characterised, and this has been correlated with powder performance on subsequent LPBF processing. It has been shown that
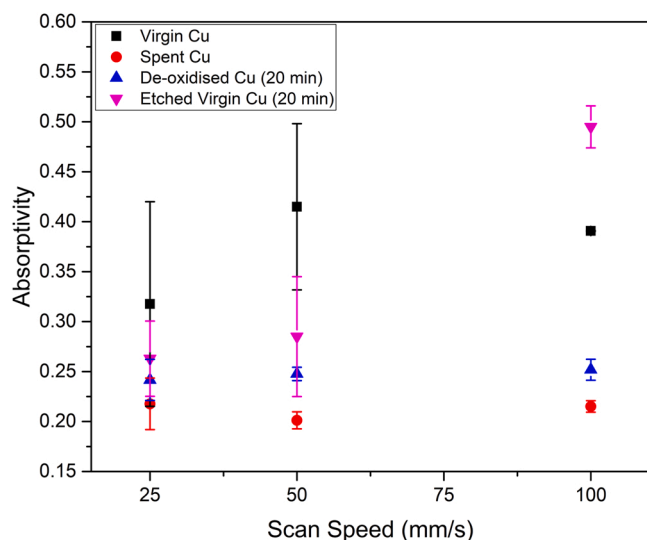
Fig. 11. Apparent absorptivity of Cu powders during LPBF. Error bars are the standard deviation from the mean of three separate tracks at each parameter.

deposits fabricated from Spent Cu powder are characterised by extensive large-scale (e.g. >50 μm) pores caused by the vaporisation and thermal decomposition of the preceding oxidised layers, which are likely composed of CuO and Cu(OH)$_2$. The presence of these large-scale pores in fabricated deposits can be eliminated by chemically reprocessing Spent Cu using conventional chemical etchants that remove thick oxide layers.

CRediT authorship contribution statement

James W. Murray: Writing – review & editing, Investigation. **Adam T. Clare:** Funding acquisition, Writing – review & editing. **Alistair Speidel:** Conceptualization, Investigation, Methodology, Writing – original draft. **Leonidas Gargalis:** Writing – review & editing, Investigation, Data curation. **Manyalibo J. Matthews:** Writing – review & editing, Funding acquisition. **Jianchao Ye:** Data curation, Writing – review & editing. **Richard Hague:** Writing – review & editing, Funding acquisition. **Adriaan Spierings:** Writing – review & editing.

Declaration of Competing Interest

The authors declare that they have no known competing financial interests or personal relationships that could have appeared to influence the work reported in this paper.

References

[1] Z.A. Young, Q. Guo, N.D. Parab, C. Zhao, M. Qu, L.I. Escano, K. Fezzaa, W. Everhart, T. Sun, L. Chen, Types of spatter and their features and formation mechanisms in laser powder bed fusion additive manufacturing process, Addit. Manuf. 36 (2020), 101438, https://doi.org/10.1016/j.addma.2020.101438.

[2] A.N.D. Gasper, B. Szost, X. Wang, D. Johns, S. Sharma, A.T. Clare, I.A. Ashcroft, Spatter and oxide formation in laser powder bed fusion of Inconel 718, Addit. Manuf. 24 (2018) 446–456, https://doi.org/10.1016/j.addma.2018.09.032.

[3] J.A. Slotwinski, E.J. Garboczi, P.E. Stutzman, C.F. Ferraris, S.S. Watson, M.A. Peltz, Characterization of metal powders used for additive manufacturing, J. Res. Natl. Inst. Stand. Technol. 119 (2014) 460, https://doi.org/10.6028/jres.119.018.

[4] A. Strondl, O. Lyckfeldt, H. Brodin, U. Ackelid, Characterization and control of powder properties for additive manufacturing, JOM 67 (2015) 549–554, https://doi.org/10.1007/s11837-015-1304-0.

[5] H. Irrinki, M. Dexter, B. Barmore, R. Enneti, S. Pasebani, S. Badwe, J. Stitzel, R. Malhotra, S.V. Atre, Effects of powder attributes and laser powder bed fusion (L-PBF) process conditions on the densification and mechanical properties of 17-4 PH stainless steel, JOM 68 (2016) 860–868, https://doi.org/10.1007/s11837-015-1770-4.

[6] L. Haferkamp, A. Spierings, M. Rusch, D. Jermann, M.A. Spurek, K. Wegener, Effect of Particle size of monomodal 316L powder on powder layer density in powder bed fusion, Prog. Addit. Manuf. (2020), https://doi.org/10.1007/s40964-020-00152-4.

[7] J. Dawes, R. Bowerman, R. Trepleton, Introduction to the additive manufacturing powder metallurgy supply chain, Johns. Matthey Technol. Rev. 59 (2015) 243–256, https://doi.org/10.1595/205651315×688686.

[8] V. Petrovic, J. Vicente Haro Gonzalez, O. Jordá Ferrando, J. Delgado Gordillo, J. Ramón Blasco Puchades, L. Portolés Griñan, Additive layered manufacturing: sectors of industrial application shown through case studies, Int. J. Prod. Res. 49 (2011) 1061–1079, https://doi.org/10.1080/00207540903479786.

[9] J. Faludi, M. Baumers, I. Maskery, R. Hague, Environmental impacts of selective laser melting: do printer, powder, or power dominate? J. Ind. Ecol. 21 (2017) S144–S156, https://doi.org/10.1111/jiec.12528.

[10] D. Powell, A.E.W. Rennie, L. Geekie, N. Burns, Understanding powder degradation in metal additive manufacturing to allow the upcycling of recycled powders, J. Clean. Prod. 268 (2020), 122077, https://doi.org/10.1016/j.jclepro.2020.122077.

[11] M.I. Boulos, New frontiers in thermal plasmas from space to nanomaterials, Nucl. Eng. Technol. 44 (2012) 1–8, https://doi.org/10.5516/NET.77.2012.001.

[12] Z. Feng, C.R. Marks, A. Barkatt, Oxidation-rate excursions during the oxidation of copper in gaseous environments at moderate temperatures, Oxid. Met. 60 (2003) 393–408, https://doi.org/10.1023/A:1027331605417.

[13] S.J. Raab, R. Guschlbauer, M.A. Lodes, C. Körner, Thermal and electrical conductivity of 99.9% pure copper processed via selective electron beam melting, Adv. Eng. Mater. 18 (2016) 1661–1666, https://doi.org/10.1002/adem.201600078.

[14] S.D. Jadhav, P.P. Dhekne, S. Dadbakhsh, J.-P. Kruth, J. Van Humbeeck, K. Vanmeensel, Surface modified copper alloy powder for reliable laser-based additive manufacturing, Addit. Manuf. 35 (2020), 101418, https://doi.org/10.1016/j.addma.2020.101418.

[15] L. Gargalis, J. Ye, M. Strantza, A. Rubenchik, J.W. Murray, A.T. Clare, I.A. Ashcroft, R. Hague, M.J. Matthews, Determining processing behaviour of pure Cu in laser powder bed fusion using direct micro-calorimetry, J. Mater. Process. Technol. 294 (2021), 117130, https://doi.org/10.1016/j.jmatprotec.2021.117130.

[16] C. Silbernagel, L. Gargalis, I. Ashcroft, R. Hague, M. Galea, P. Dickens, Electrical resistivity of pure copper processed by medium-powered laser powder bed fusion additive manufacturing for use in electromagnetic applications, Addit. Manuf. 29 (2019), 100831, https://doi.org/10.1016/j.addma.2019.100831.

[17] M. Abdelhafiz, K.S. Al-Rubaie, A. Emadi, M.A. Elbestawi, Process–structure–property relationships of copper parts manufactured by laser powder bed fusion, Materials (2021) 2945, https://doi.org/10.3390/ma14112945.

[18] C. Salvan, L. Briottet, T. Baffie, L. Guetaz, C. Flament, CuCrZr alloy produced by laser powder bed fusion: microstructure, nanoscale strengthening mechanisms, electrical and mechanical properties, Mater. Sci. Eng. A 826 (2021), 141915, https://doi.org/10.1016/j.msea.2021.141915.

[19] S.D. Jadhav, S. Dadbakhsh, L. Goossens, J.-P. Kruth, J. Van Humbeeck, K. Vanmeensel, Influence of selective laser melting process parameters on texture evolution in pure copper, J. Mater. Process. Technol. 270 (2019) 47–58, https://doi.org/10.1016/j.jmatprotec.2019.02.022.

[20] S.D. Jadhav, D. Fu, M. Deprez, K. Ramharter, D. Willems, B. Van Hooreweder, K. Vanmeensel, Highly conductive and strong CuSn0.3 alloy processed via laser powder bed fusion starting from a tin-coated copper powder, Addit. Manuf. 36 (2020), 101607, https://doi.org/10.1016/j.addma.2020.101607.

[21] V. Lindström, O. Liashenko, K. Zweiacker, S. Derevianko, V. Morozovych, Y. Lyashenko, C. Leinenbach, Laser powder bed fusion of metal coated copper powders, Materials 13 (2020) 3493, https://doi.org/10.3390/ma13163493.

[22] P. Lassègue, C. Salvan, E. De Vito, R. Soulas, M. Herbin, A. Hemberg, T. Godfroid, T. Baffie, G. Roux, Laser powder bed fusion (L-PBF) of Cu and CuCrZr parts: influence of an absorptive physical vapor deposition (PVD) coating on the printing process, Addit. Manuf. 39 (2021), 101888, https://doi.org/10.1016/j.addma.2021.101888.

[23] A. Speidel, M.D. Wadge, L. Gargalis, T.P. Cooper, W. Reynolds, D. Grant, R. Hague, A.T. Clare, J.W. Murray, The interaction of volatile metal coatings during the laser powder bed fusion of copper, J. Mater. Process. Technol. 299 (2022), 117332, https://doi.org/10.1016/j.jmatprotec.2021.117332.

[24] S.D. Jadhav, J. Vleugels, J. Kruth, J. Van Humbeeck, K. Vanmeensel, Mechanical and electrical properties of selective laser-melted parts produced from surface-oxidized copper powder, Mater. Des. Process. Commun. 2 (2020), https://doi.org/10.1002/mdp2.94.

[25] J. Wendel, S.K. Manchili, E. Hryha, L. Nyborg, Oxide reduction and oxygen removal in water-atomized iron powder: a kinetic study, J. Therm. Anal. Calorim. 142 (2020) 309–320, https://doi.org/10.1007/s10973-020-09724-6.

[26] J.W. Murray, M. Simonelli, A. Speidel, D.M. Grant, A.T. Clare, Spheroidisation of metal powder by pulsed electron beam irradiation, Powder Technol. 350 (2019) 100–106, https://doi.org/10.1016/j.powtec.2019.03.041.

[27] Q. Bao, Y. Yang, X. Wen, L. Guo, Z. Guo, The preparation of spherical metal powders using the high-temperature remelting spheroidization technology, Mater. Des. 199 (2021) 109382, https://doi.org/10.1016/j.matdes.2020.109382.

[28] W.-H. Wei, L.-Z. Wang, T. Chen, X.-M. Duan, W. Li, Study on the flow properties of Ti-6Al-4V powders prepared by radio-frequency plasma spheroidization, Adv. Powder Technol. 28 (2017) 2431–2437, https://doi.org/10.1016/j.apt.2017.06.025.

[29] G. Nordet, C. Gorny, Y. Mayi, J. Daligault, M. Dal, A. Effernelli, E. Blanchet, F. Coste, P. Peyre, Absorptivity measurements during laser powder bed fusion of pure copper with a 1 kW cw green laser, Opt. Laser Technol. 147 (2022), 107612, https://doi.org/10.1016/j.optlastec.2021.107612.

[30] A.T. Clare, W.J. Reynolds, J.W. Murray, N.T. Aboulkhair, M. Simonelli, M. Hardy, D.M. Grant, C. Tuck, Laser calorimetry for assessment of melting behaviour in multi-walled carbon nanotube decorated aluminium by laser powder bed fusion, CIRP Ann. 69 (2020) 197–200, https://doi.org/10.1016/j.cirp.2020.04.053.

[31] J. Trapp, A.M. Rubenchik, G. Guss, M.J. Matthews, In situ absorptivity measurements of metallic powders during laser powder-bed fusion additive manufacturing, Appl. Mater. Today 9 (2017) 341–349, https://doi.org/10.1016/j.apmt.2017.08.006.

[32] K. Ujihara, Reflectivity of metals at high temperatures, J. Appl. Phys. 43 (1972) 2376–2383, https://doi.org/10.1063/1.1661506.

[33] S. Suzuki, Y. Ishikawa, M. Isshiki, Y. Waseda, Native oxide layers formed on the surface of ultra high-purity iron and copper investigated by angle resolved XPS, Mater. Trans. JIM 38 (1997) 1004–1009, https://doi.org/10.2320/matertrans1989.38.1004.

[34] M.C. Biesinger, L.W.M. Lau, A.R. Gerson, R.S.C. Smart, Resolving surface chemical states in XPS analysis of first row transition metals, oxides and hydroxides: Sc, Ti,

V, Cu and Zn, Appl. Surf. Sci. 257 (2010) 887–898, https://doi.org/10.1016/j.apsusc.2010.07.086.

[35] M.C. Biesinger, Advanced analysis of copper X-ray photoelectron spectra, Surf. Interface Anal. 49 (2017) 1325–1334, https://doi.org/10.1002/sia.6239.

[36] R. Hajimammadov, Z. Csendes, J.-M. Ojakoski, G.S. Lorite, M. Mohl, K. Kordas, Nonlinear electronic transport and enhanced catalytic behavior caused by native oxides on Cu nanowires, Surf. Sci. 663 (2017) 16–22, https://doi.org/10.1016/j.susc.2017.04.011.

[37] J.-C. Dupin, D. Gonbeau, P. Vinatier, A. Levasseur, Systematic XPS studies of metal oxides, hydroxides and peroxides, Phys. Chem. Chem. Phys. 2 (2000) 1319–1324, https://doi.org/10.1039/a908800h.

[38] Y. Cudennec, A. Lecerf, The transformation of Cu(OH)2 into CuO, revisited, Solid State Sci. 5 (2003) 1471–1474, https://doi.org/10.1016/j.solidstatesciences.2003.09.009.

[39] H. Demir, C. Özmetin, M.M. Kocakerim, S. Yapıcı, M. Çopur, Determination of a semi empirical kinetic model for dissolution of metallic copper particles in HNO3 solutions, Chem. Eng. Process. Process. Intensif. 43 (2004) 1095–1100, https://doi.org/10.1016/j.cep.2003.11.002.

[40] M.J. Heiden, L.A. Deibler, J.M. Rodelas, J.R. Koepke, D.J. Tung, D.J. Saiz, B. H. Jared, Evolution of 316L stainless steel feedstock due to laser powder bed fusion process, Addit. Manuf. 25 (2019) 84–103, https://doi.org/10.1016/j.addma.2018.10.019.

[41] R. Williams, M. Bilton, N. Harrison, P. Fox, The impact of oxidised powder particles on the microstructure and mechanical properties of Ti-6Al-4 V processed by laser powder bed fusion, Addit. Manuf. 46 (2021), 102181, https://doi.org/10.1016/j.addma.2021.102181.

[42] A.T. Clare, R.S. Mishra, M. Merklein, H. Tan, I. Todd, L. Chechik, J. Li, M. Bambach, Alloy design and adaptation for additive manufacture, J. Mater. Process. Technol. 299 (2022), 117358, https://doi.org/10.1016/j.jmatprotec.2021.117358.